

Contents lists available at ScienceDirect

### **Applied Surface Science**

journal homepage: www.elsevier.com



Full Length Article

# VO<sub>2</sub> nanoparticles on edge orientated graphene foam for high rate lithium ion batteries and supercapacitors

Guofeng Ren\*, Ruibo Zhang, Zhaoyang Fan\*

Department of Electrical and Computer Engineering and Nano Tech Center, Texas Tech University, Lubbock, Texas 79409, USA

#### ARTICLE INFO

Article history:
Received 4 September 2017
Received in revised form 29 January 2018
Accepted 5 February 2018
Available online xxx

Keywords:
High rate lithium ion batteries
High rate supercapacitors
Graphene foam
Vanadium oxide

#### ABSTRACT

With the fully exposed graphene edges, high conductivity and large surface area, edge oriented graphene foam (EOGF), prepared by deposition of perpendicular graphene network encircling the struts of Ni foam, is a superior scaffold to support active materials for electrochemical applications. With VO<sub>2</sub> as an example, EOGF loaded VO<sub>2</sub> nanoparticle (VO<sub>2</sub>/EOGF) electrode has high rate performance as cathode in lithium ion batteries (LIBs). In addition to the Li<sup>+</sup> intercalation into the lattice, contribution of non-diffusion-limited pseudocapacitance to the capacity is prominent at high rates. VO<sub>2</sub>/EOGF based supercapacitor also exhibits fast response, with a characteristic frequency of 15 Hz when the phase angle reaches  $^-45^\circ$ , or a relaxation time constant of 66.7 ms. These results suggest the promising potential of EOGF as a scaffold in supporting active nanomaterials for electrochemical energy storage and other applications.

© 2017.

#### 1. Introduction

Transition metal oxides are commonly used as the electrochemical active materials for supercapacitors and lithium-ion batteries. However, several challenges, particularly their poor electronic and ionic conductivities and typically small specific surface area prohibit their direct application in high-performance energy storage devices. Anchoring metal oxide nanoparticles (NPs) on graphene nanosheets to form composites, leveraging the high conductivity of graphene and its large surface area and simultaneously preventing oxide NPs agglomeration, has been extensively explored in recent years [1–10]. Graphene (or thin-graphite) foam (GF) prepared by chemical vapor deposition (CVD) of multilayer graphene on a nickel foam, has attracted huge interests [11], due to its potentials to tackle overcome several issues related to the discrete chemically-derived tiny graphene nanosheets, such as their limited conductivity, large inter-sheet resistance, and restacking of sheets. Such GF is a continuous conductive framework that has well-connected graphene layers and can be applied as a free-standing electrode without extra current collector. Therefore, it is not surprising that using GF as the framework to support active oxides to construct nanostructured electrodes, supercapacitors and lithium ion batteries (LIBs) can achieve high performance, especially high charge-discharge rate and high power performances [12-15]. This is because such a nanostructured electrode can minimize ion diffusion length, increase the interface between electrolyte and electrode, and provide rapid electron conducting paths and robust mechanical support, in addition to others.

Email addresses: Guofeng.Ren@ttu.edu (G. Ren); Zhaoyang.Fan@ttu.edu (Z. Fan)

However, these previously reported GFs have a very limited surface area since graphene layers are conformably (or laterally) deposited on the nickel foam template, which itself has a very small surface area. Therefore, a thick active mass coating or orthogonally-grown nanorod/nanowire structure [14,15] must be applied on the struts of lateral GF. It has no doubt that this thick active layer limits the device kinetic performance. Furthermore, graphene edges, chemically-active "hot" spots for oxides nucleation and growth, are buried in the lateral layers, and therefore are not easily accessible.

Vertically oriented graphene (VOG), synthesized by plasma enhanced CVD (PECVD) on a flat substrate, has well opened porous structure, high conductivity, large surface area, and fully-exposed graphene edges. VOG has diverse applications [16,17], including high-frequency electric double layer capacitor (EDLC) [18-20], LIBs [21,22] and lithium sulfur batteries [23]. To tackle the problems of lateral GF, VOG structure grown around a 3D Ni foam substrate with the perpendicular graphene sheets encircling the underlying Ni strut, or the so-called perpendicular edge oriented graphene foam (EOGF) is promising [24]. In EOGF, graphene sheets first grow laterally along Ni strut surface and then bend to the perpendicular orientation, thus with a much larger surface area than the lateral GF and with graphene edges fully exposed. When it was used for EDLC, kilohertz rate performance was demonstrated [25]. In this work, EOGF loaded with active materials is demonstrated to be a promising free-standing electrode for LIBs and supercapacitors. In the field of metal oxide active materials, vanadium oxides including VO2 and V2O5, have been widely studied for LIBs and supercapacitors due to their abundance in nature, low cost and a reasonable large capacity [26-29]. Herein, VO2 NPs anchored on EOGF was studied as electrodes for high-rate pseudocapacitors and LIBs.

<sup>\*</sup> Corresponding authors.

#### 2. Experiments

EOGF synthesis: EOGF was synthesized by microwave PECVD with  $CH_4$  and  $H_2$  as gases and nickel foam as the template. After a brief  $H_2$  plasma cleaning, EOG was deposited with 50 sccm  $CH_4$  and 100 sccm  $H_2$  gas flow for around 10 min. The detail synthesis method can be found in our previous study [25].

Synthesis of VO<sub>2</sub> NPs on EOGF: Vanadyl acetylacetonate (VO(acac)<sub>2</sub>) was employed as precursor to deposit VO<sub>2</sub> on EOGF. First, 265 mg VO(acac)<sub>2</sub> was dissolved into 95 ml ethanol and stirred for 24 h. 5 ml deionized water was then added to the solution. After that, 100 ml of the solution was poured into a 125 ml Teflon lined autoclave with a 50 mg EOGF loaded. The synthesis was conducted in an oven at 180 °C for 20 h. After cooling down, the sample was washed with ethanol for several times and dried under vacuum at 80 °C for 20 h. It was then annealed in nitrogen at 350 °C for 2 h. The mass of vanadium oxide coated on EOGF was determined by mass difference before and after oxide deposition using a balance with a precision of 0.002 mg. The vanadium oxide coated EOGF (VO<sub>2</sub>/EOGF) was used as a freestanding electrode directly without any conductive additives and binders.

#### 2.1. Materials characterization

The morphology and microstructure of the electrode was characterized by scanning electron microscopy (SEM) and transmission electron microscope (TEM). Raman spectroscopy, energy dispersive X-ray spectra (EDX) and powder X-ray diffraction (XRD) were used to determined chemical components and crystal structure.

#### 2.2. Battery assembly and electrochemical measurements

The as-prepared electrodes were assembled into CR-3032 coin cells with a separator and a lithium chip counter electrode in an argon filled glovebox that had both moisture and oxygen concentrations below 0.1 ppm. 1 M LiPF<sub>6</sub> in ethylene carbonate, diethyl carbonate and dimethyl carbonate (1:1:1 by volume) was used as the electrolyte. The assembled coin cell was rested in the glovebox for 12 h before electrochemical measurements. A Bio-Logic electrochemical workstation was employed to characterize the capacitive performance of the assembled coin cells including cyclic voltammetry (CV) and electrochemical impedance spectroscopy (EIS). A small current density of  $0.3 \,\mathrm{mA \, g^{-1}}$ , based on the active mass of  $\mathrm{VO}_2$ , was used in the first charge-discharge cycle to activate the cell. CV measurement of the assembled cell was carried out over a voltage range of 1.5-3.5 V and at different scan rates from 1 mV s<sup>-1</sup> to 100 mV s<sup>-1</sup>. Galvanostatic charge-discharge (C-D) measurement of the battery cell was carried out at different current densities from  $0.5 \,\mathrm{Ag^{-1}}$  to  $50 \,\mathrm{Ag^{-1}}$  by a LAND CT-2001A battery test system. The cycling stability of the electrode was tested based on C-D measurement at a current density of 8 A g for 150 cycles. EIS measurement was carried out in the frequency ranging from 1 Hz to 100 kHz with 5 mV alternating current amplitude under a bias voltage of 2.5 V.

#### 2.3. Pseudocapacitor assembly and electrochemical measurements

Two as-fabricated  $VO_2/EOGF$  electrodes were first wetted in 5 M LiCl aqueous solution in vacuum and then assembled into a stainless coin cell (CR2016) with a 25  $\mu$ m separator (Celgard 3501). A Bio-Logic electrochemical workstation was employed to explore the capacitive performance of the assembled coin cells including CV, C-D and EIS. Bare EOGF without  $VO_2$  coating was also tested for comparison. CV measurement was carried out over voltage range 0–0.8 V and at different scan rates from  $2\,\mathrm{mV\,s}^{-1}$  to  $1000\,\mathrm{mV\,s}^{-1}$ . C-D measurement

surement was carried out at different current densities from  $1\,\mathrm{A\,g}^{-1}$  to  $50\,\mathrm{A\,g}^{-1}$ . EIS measurement was conducted over frequency range from  $100\,\mathrm{kHz}$  to  $10\,\mathrm{mHz}$ , with  $5\,\mathrm{mV}$  alternating current under a bias voltage of  $0\,\mathrm{V}$ . The long-term stability of the  $\mathrm{VO}_2/\mathrm{EOGF}$  supercapacitors were tested via C-D cycling for 1500 cycles.

#### 3. Results and discussions

#### 3.1. Morphology characterization and chemical analysis

Electron microscopic images of EOGF and VO<sub>2</sub>/EOGF are shown in Fig. 1. SEM images in Fig. 1(a) shows the overall EOGF morphology at large scales (low magnifications), indicating the 3–4 layers of foam structure with approximately 100 um large pores and tens of um wide struts. Multilayer graphene (or thin graphite) first grew laterally along the surface of nickel struts and then perpendicularly to form EOGF. EOG covers all the surface surrounding nickel struts. The smaller scale view in Fig. 1(b) presents the maze-like structure formed by the perpendicular graphene sheet network. Small flakes growing from large flakes further enlarge the surface area. TEM images in Fig. 1(c) shows the detail morphology of these sheets with sharp tips, and the high-resolution image of EOG flake clearly displays the tapered shape with a wider base and a narrower tip, and along the vertical wall redistributed with fully exposed graphene edges. The excellent conductivity of graphene flakes and the close interconnection between flakes ensures a highly conductive framework, and meanwhile the open structure with large surface area will facilitate the loading of active materials and the migration of electrolyte ions. Such an EOGF, with the unique combination of several merits that include high conductivity, large surface area, free electrolyte pathway, and robust mechanical structure, can act as an idea framework to load oxides or other active materials for electrochemical applications including electrochemical sensors, fuel cells, dye sensitized solar cells, supercapacitors and LIBs. As shown in Fig. 1d, VO2 NPs were uniformly anchored along EOG flakes. These VO2 NPs were formed through hydrolysis of VO(acac)<sub>2</sub> precursor [30]. As shown in Fig. S1 in the Supplementary Information (SI), when VO(acac)<sub>2</sub> was initially mixed with ethanol, the solution had a dark green color, which gradually changed to dark brown with stirring for 24 h, suggesting reduction of  $V^{5+}$  to  $V^{4+}$  [31]. In the subsequent hydrothermal process, defects in EOG flakes, including those fully-exposed highly-dense graphene edges, due to their unsaturated chemical bonds, acted as nucleation sites of VO2 and subsequently they grew into NPs that are tightly anchored on EOG walls.

XRD measurement of VO<sub>2</sub> without EOGF, shown in Fig. 2a, indicates that the synthesized vanadium oxide is a mixture of VO<sub>2</sub>(B) and VO<sub>2</sub>(M) phases. VO<sub>2</sub>(B) has a layered structure composed of edge sharing VO<sub>6</sub> octahedra units connected by corner sharing to neighboring layers along the c-direction of the VO<sub>6</sub> octahedra. VO<sub>2</sub>(M) is also composed of VO<sub>6</sub> octahedra units but has a monoclinically distorted rutile structure. XRD peaks from VO<sub>2</sub> is not intense, which is probably because the particle size is small and crystallization is not good. Raman spectra of EOGF and VO<sub>2</sub>/EOGF are plotted in Fig. 2b and c. The characteristic D (1355 cm<sup>-</sup>), G (1586 cm<sup>-1</sup>), D' (1629 cm<sup>-1</sup>), 2D (2701 cm<sup>-1</sup>), and 2D' (3253 cm<sup>-1</sup>) bands of graphene/ graphite are shown as green line in Fig. 2b. G peak and 2D peak from graphene [32] and the intensity ratio (3.7) of the 2D and G peak implies that EOGF consist of few to multiple layers of graphene [11,33], consistent to the TEM image in Fig. 1(c). The relatively strong defect-related D peak can be explained by the fully exposed defective graphene edges of EOG and other plasma-induced defects, further confirmed by the clearly discernible shoulder D' peak of the G band, which comes from graphene defects, including edges [34]. For VO<sub>2</sub>/EOGF samples, in addition to those graphene peaks, peaks at

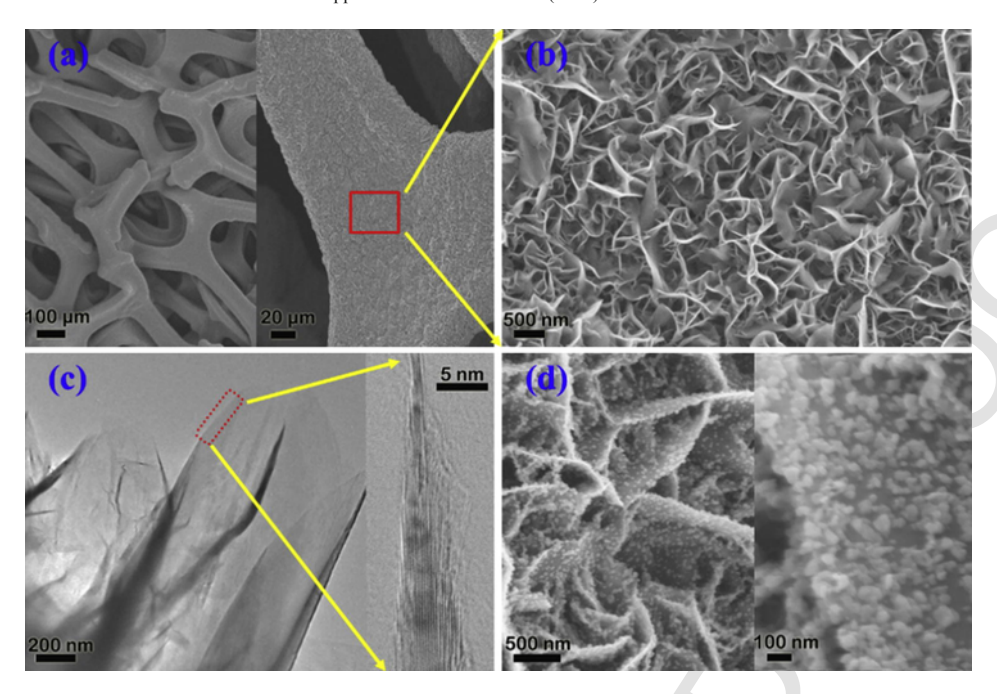


Fig. 1. (a) SEM images of EOGF at two different magnifications. (b) SEM image of EOG flake network. (c) TEM images of EOG flakes (left) and cross sectional high-resolution image of EOG flakes. (d) SEM images of VO<sub>2</sub> on EOG at two different magnifications.

142, 199, 228, 265, 315, 344, 395, 500, and 618 cm<sup>-1</sup> are from vanadium oxide [35–37]. VO<sub>2</sub> nanoparticles synthesized from the same autoclave where VO<sub>2</sub>/EOGF from was deposited on a substrate and EDX was carried out to investigate the chemical components of the sample. From the obtained EDX data, it was found that V to O ratio is roughly 1:2. Considering the data from XRD, EDX and Raman spectra, the nanoparticles are believed to be VO<sub>2</sub>.

#### 3.2. Electrochemical studies of VO<sub>2</sub>/EOGF electrode for LIBs

After assembling the VO<sub>2</sub>/EOGF electrode into a coin cell with Li as the counter electrode, CV, C-D and EIS studies were performed to investigate its electrochemical properties. The charge storage in EOGF itself is exclusively between the potential range of 0–1 V (vs. Li/Li<sup>+</sup>) with negligible capacity above 1 V [24]. Therefore in the following the measured capacity of VO<sub>2</sub>/EOGF electrode in the potential range of 1.5–3.5 V is considered to be exclusively contributed by VO<sub>2</sub>.

CV curves of the cell at a few representative scan rates of 5, 10, 50, and 100 mAh g<sup>-1</sup> are presented in Fig. 3a and S3a. As shown, the measured current, and hence the integral area of CV curves increases with the scan rate increases. For low scan rates such as 5 mV/s, anodic peaks at 2.37 V and 2.73 V and cathodic peaks at 2.00 V and 2.45 V are visible. The higher anodic peak at 2.73 V and higher cathodic peak at 2.45 V is consistent with CV curves of VO<sub>2</sub>(B) in lithium ion battery reported [38,39]. The arising of additional peaks might be caused by morphology and prepared process of VO<sub>2</sub> since VO<sub>2</sub>(M) impurity was found [40] These peaks are not very sharp, correspondingly, there are no obvious plateaus on C-D curves plotted in Fig. 3b. This phenomenon suggests a significant contribution of pseudocapacitive storage by VO<sub>2</sub> NPs to the total charge storage, as will be analyzed later. With scan rate increases, anodic peaks shift right and cathodic peaks shift left due to polarization. At a higher scan rate of 100 mAh g<sup>-1</sup> (Fig. S3a), the peaks become almost indiscernible.

VO<sub>2</sub>/EOGF nanostructured electrode exhibits high rate performance and large specific capacity, confirmed by C-D measurements

at different current densities up to  $50\,\mathrm{Ag}^{-1}$  (Fig. 3b). The discharge capacity at different rates and its cycling stability are further presented in Fig. 3c, with six C-D cycles at each rate. At a lower discharge current density of  $0.5\,\mathrm{A\,g}^{-1}$ ,  $\mathrm{VO_2}$  NPs exhibit a specific capacity of  $300\,\mathrm{mAh\,g}^{-1}$ . This is considerably larger than previously reported specific capacity that is in the range of 200–250 mAh g<sup>-1</sup> measured at same current density for bulk VO2 or VO2 microscale particles [29,38,39,41]. As will be discussed, in addition to Li<sup>+</sup> intercalation into the lattice, surface-related pseudocapacitance contributes a significant extra part to the measured total capacity. At 20 A g<sup>-1</sup>, our VO<sub>2</sub>/EOGF electrode maintains a specific capacity of 144 mAh g<sup>-1</sup>. A capacity of 91 mAh g<sup>-1</sup> still remains at a discharge current as large as 50 A g<sup>-1</sup>. Compared with reduced graphene oxide (RGO) coupled with metal oxides including  $TiO_2$  (98 mAh g<sup>-1</sup> at 10 A g<sup>-1</sup>) [42],  $VO_2$  $(102 \,\mathrm{mAh}\,\mathrm{g}^{-1} \,\mathrm{at}\, 5\,\mathrm{A}\,\mathrm{g}^{-}) \,[43], \,\mathrm{Fe_2O_3} \,(700 \,\mathrm{mAh}\,\mathrm{g}^{-1} \,\mathrm{at}\, 0.8\,\mathrm{A}\,\mathrm{g}^{-}) \,[44],$  $Co_3O_4$  (480 mAh g<sup>-1</sup> at 0.5 A g<sup>-</sup>) [45],  $VO_2$ /EOGF can work at much higher rate due to its unique nanostructure and high conductivity. Cycling stability plotted in Fig. 3d was carried out at a current density of 8 A g<sup>-1</sup> for 150 cycles, which shows an almost 100% Coulombic efficiency in every cycle and 90% capacity remains at the end of cycling. These studies suggest that EOGF be a promising framework for supporting active materials to produce freestanding electrodes for lithium ion battery.

To shed light on the superior rate performance of VO<sub>2</sub>/EOGF, EIS measurement was conducted to acquire the electrode resistance and charge transfer resistance. The Nyquist plot and the equivalent circuit used to model the impedances are shown in Fig. S4, where  $R_1$  represents the ohmic resistance,  $R_2$  represents the charge transfer resistance,  $W_2$  is the Warburg impedance and constant phase element  $Q_2$  relates to the interfacial capacitance [46]. The extracted ohmic resistance  $R_1$  and charge transfer resistance  $R_2$  are  $3.7\Omega$  and  $23\Omega$  respectively, much less than electrodes based on RGO coupled TiO<sub>2</sub> ( $R_2 \sim 70\Omega$ ) [42] and 3D RGO coupled with Fe<sub>2</sub>O<sub>3</sub> ( $R_2 \sim 95\Omega$ ) [47]. The small resistances of the VO<sub>2</sub>/EOGF electrode provides the basis for the measured high rate performance. These results confirm that the unique structure and properties of the VO<sub>2</sub>/EOGF electrode facilitate Li<sup>+</sup> migration and intercalation as well as electron transport in the

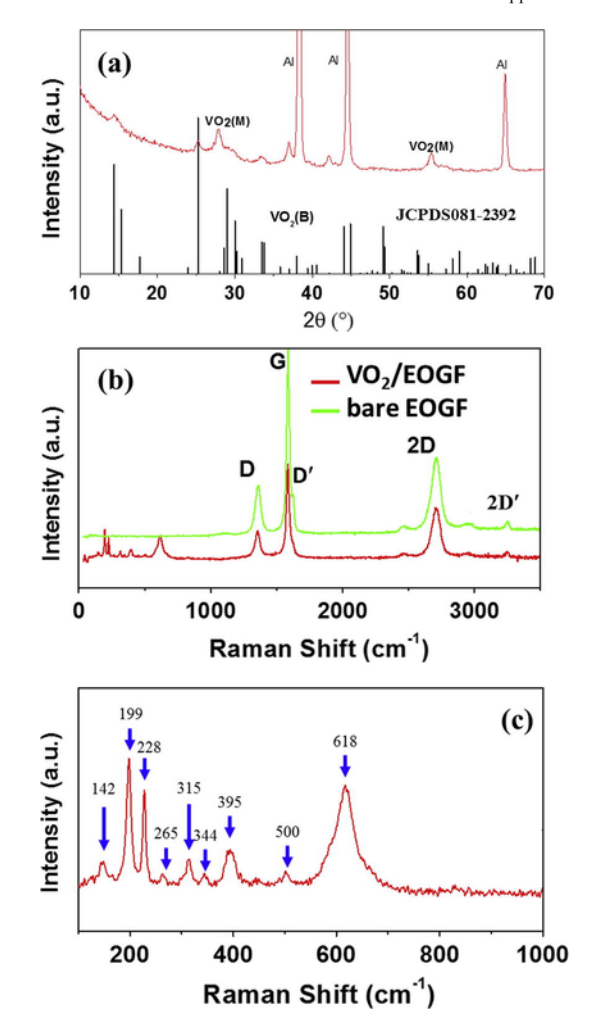


Fig. 2. (a) XRD pattern of the synthesized  $VO_2$  and the standard  $VO_2(B)$  phase pattern (JCPDS Card No.081-2392). The three strong peaks are from an aluminum sample holder used in the measurement. (b) Raman spectra of EOGF and  $VO_2$ /EOGF. (c) Zoom-in view of Raman spectrum of  $VO_2$ /EOGF in region of 100–1000 cm<sup>-1</sup> to show  $VO_2$  related peaks.

electrode. Since the diffusion time is proportional to the square of the diffusion distance, NPs can significantly shorten the diffusion (intercalation/deintercalation) time of lithium ion in the oxide lattice by reducing the diffusion distance. EOGF, with its stable porous structure, large surface area and high conductivity over the entire scaffold, provides free pathways for lithium ion and electrolyte diffusion, surface area to support nanoscale materials and conductive framework for electron transportation.

Since VO<sub>2</sub> NPs possesses considerable pseudocapacitive effect [48], it is necessary to differentiate the charge storage mechanisms in the VO<sub>2</sub> NPs based LIB electrode to better understand its superior rate performance and other properties. It is known that for nanostructured electrodes, in addition to the charge storage due to Li<sup>+</sup> intercalation in the "bulk" lattice that is a diffusion-limited process, the large surface area of active nanomaterials also contributes considerable amount of storage capacity due to the surface-related pseudocapacitance (and to a less extent, the double layer capacitance). Comparing to the intercalation process, this pseudocapacitance contribution will be more pronounced at high rates since it is a non-diffusion-limited facile Faradic effect occurring at the surface or subsurface of the active oxide NPs. CV study was used to differentiate contributions from capacitance and intercalation through currents (*i*) mea-

sured at different scan rates (v), as described in the SI. As an approximation, the charge storage capacity originating from capacitive effect  $(C_c)$  does not depend on the scan rate in the ideal case, and therefore pseudocapacitive storage capacity roughly remains constant even at higher C-D current densities. Thus, a large surface area, by providing a large pseudocapacitance, is in favor of high-rate performance by contributing a constant  $C_c$ . On the other hand, the capacity  $C_i$  originating from bulk intercalation decreases with the increment of scan rate. Therefore, when the C-D rate is high enough,  $C_i$  will become negligible due to slow diffusion in the bulk lattice, and the total capacity of the activated materials can be considered only determined by the surface-determined pseudocapacitive storage.

As for our VO<sub>2</sub>/EOGF electrode, the dominant cathodic peak in the CV measurement is plotted in Fig. 3e (black line) and fitted into  $i_i$  (red<sup>1</sup> line) and  $i_c$  (green line) as:

$$i = i_c + i_i = 0.29\nu + 1.55\nu^{1/2} \tag{1}$$

This fitting gives an estimation on the relative contribution of pseudocapacitive storage and bulk intercalation storage to the total capacity. From these curves, Li $^{+}$  intercalation current dominates the total current when scan rate is below  $30\,\text{mV}\,\text{s}^{-1}$ , above which, the pseudocapacitive current dominates. Extrapolation of Eq. (1) plotted in Fig. S3b shows currents at different scan rates. The contribution of pseudocapacitive storage and bulk intercalation to total capacity at different scan rates can be estimated, whose results are plotted in Fig. 3e. At low scan rate  $2\,\text{mV}\,\text{s}^{-1}$ , bulk intercalation contributes about 80% to the total capacity, while at scan rate  $300\,\text{mV}\,\text{s}^{-1}$ , it only contributes 20% of the total capacity and the remaining 80% comes from surface-related pseudocapacitance. Contribution from pseudocapacitive storage is assumed to be a constant, and it is about  $60\,\text{mAh}\,\text{g}^{-1}$ .

## 3.3. Electrochemical studies of VO<sub>2</sub>/EOGF electrode for pseudocapacitors

Symmetric cells were assembled with VO<sub>2</sub>/EOGF electrodes to test their performance for supercapacitors, 5M LiCl aqueous solution was employed as electrolyte. The performance of supercapacitors is affected by the electrolyte [49] and it was found that vanadium oxide supercapacitors are stable and negligibly soluble in high concentrated LiCl electrolyte [27]. The CV curves of bare EOG and VO<sub>2</sub>/EOGF at a representative 100 mV s<sup>-1</sup> are compared in Fig. S5, with an enclosed area ratio of 50:1, indicating the capacity contribution from EOGF itself is negligible. CV curves of VO<sub>2</sub>/EOGF at scan rates from 2 mV s<sup>-1</sup> to 1000 mV s<sup>-1</sup> are plotted in Fig. 4a. At a scan rate of 1000 mV s<sup>-1</sup>, the CV curve still maintains a desirable quasi-rectangle profile. The high rate capability of the VO<sub>2</sub>/EOGF electrode is due to the synergetic effects of the high conductivity of EOGF, small size of VO<sub>2</sub> nanoparticles and free ion pathways in the 3D structure. The capacitance of the electrode is plotted in Fig. 4b. VO<sub>2</sub>/EOGF electrode has a capacitance around two orders of magnitude larger than the bare EOGF. At a scan rate of 2 mV s<sup>-1</sup>, bare EOGF has a tiny capacitance of 2.0 mF cm<sup>-2</sup>, compared to 119 mF cm<sup>-2</sup> of VO<sub>2</sub>/EOGF electrode with a VO<sub>2</sub> mass loading of 0.5 mg. At high scan rate 1000 mV s<sup>-1</sup>, an areal capacitance of 26 mF cm<sup>-2</sup> still remains. Specific capacitance of VO<sub>2</sub> was calculated and plotted in Fig. 4c. Discharge curves and specific capacitance at different discharge current density are plotted in Fig. S6. VO<sub>2</sub> shows a specific capacitance of 300F  $g^{-1}$  at a discharge current density of  $2 A g^{-1}$ . The capacitance retention from C-D cycling at  $10 A g^{-1}$  for 1500 cycles is plotted in Fig.

<sup>&</sup>lt;sup>1</sup> For interpretation of color in Fig. 3, the reader is referred to the web version of this article.

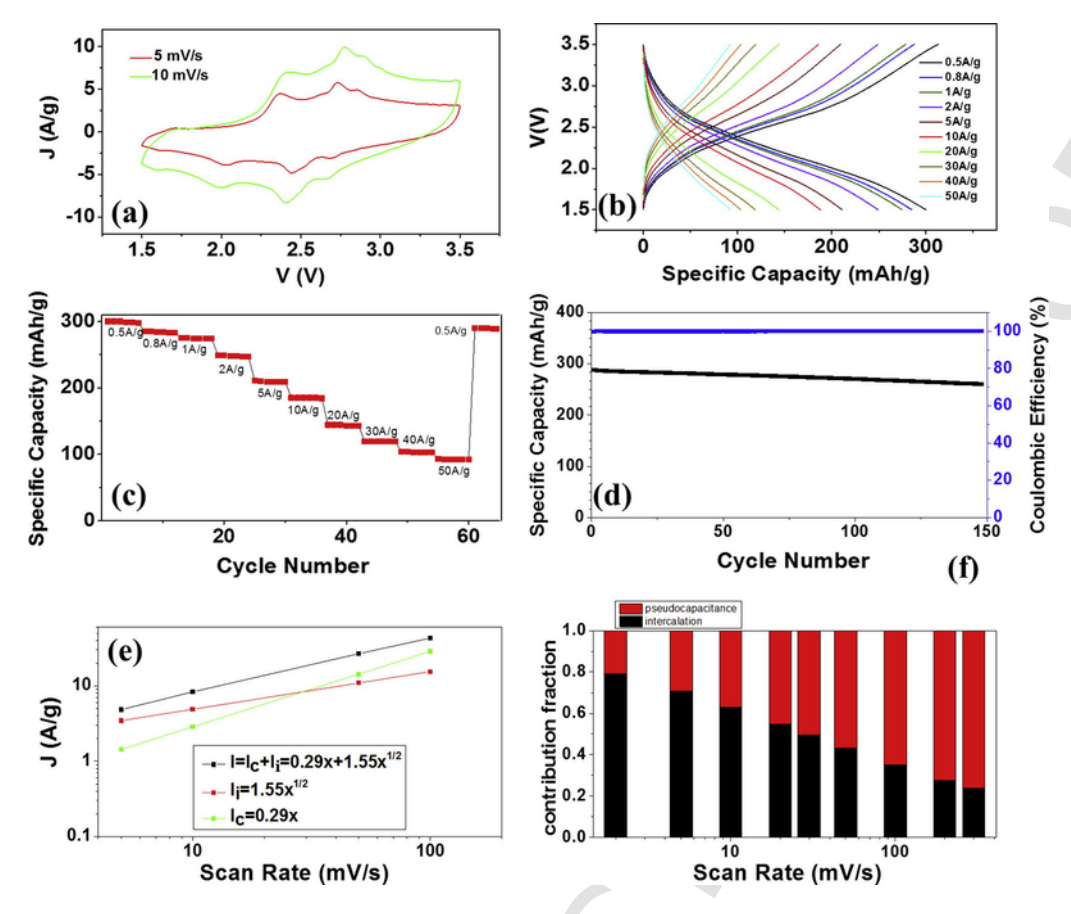


Fig. 3. Electrochemical study of  $VO_2/EOGF$  electrode in a LIB cell. (a) CV curves at low scan rates. (b) C-D curves at different current densities. (c) Rate performance and cycling performance. (d) Cycling stability and Coulombic efficiency of the cell tested at a current density of  $8Ag^{-1}$ . (f) Fitting of dominant CV cathodic peak current. (e) Contribution of non-diffusion-limited pseudocapacitance and diffusion-limited intercalation to the total capacity at different scan rates.

4d, showing 70% capacitance retention after 1500 cycles. Ragone plot in Fig. S7 compares the power density and energy density of capacitors based on diverse electrodes including graphene fiber/MnO<sub>2</sub> [50], Pen-ink/fiber [51], PANi/fiber [52] and VOG/kimwiper [19], which clearly shows the good energy density and power density of VO/EOGF

EIS results of VO<sub>2</sub>/EOGF based supercapacitors are plotted in Fig. 4e, f. The intercept of Nyquist plot (Fig. 4e) with the real axis at high frequency represents internal resistance of the cell, which is as small as  $0.26\Omega$ , indicating tight binding between the EOGF and VO<sub>2</sub> nanoparticles and high conductivity of the EOGF. The small semicircle at the medium frequency region is originated from interfacial charge transfer resistances, which is about  $0.30 \Omega$ . This small value indicates fast charge transfer between electrolyte and electrodes due to the large interfacial area of between electrolyte nanoparticles anchored on EOGF, which enhances the kinetic performance of VO<sub>2</sub>/EOGF electrodes. The steep slope of low frequency region indicates fast ion diffusion in the active materials due to the small size of nanoparticles, implying high rate properties of the electrodes. The Bode plot in Fig. 4e shows the frequency depended phase angle of the cell. Ideal capacitors without resistive loss should have a phase angle of -90°. As frequency increases, the resistive component severely deceases the absolute phase angle vale and lead to serious energy loss. The characteristic frequency when the phase angle reaches -45° represents the boundary between resistive and capacitive dominance of the cell. The cell behaves more like a capacitor at a frequency below the characteristic frequency, while it behaves more like a resistor above this frequency. Of the two categories of supercapaci-

tors, conventional EDLCs typically have a characteristic frequency value below 1 Hz, limited by their porous electrode structure, while pseudocapacitors, due to the charge transfer based storage mechanism, are even slower. However, the Bode plot shows that VO<sub>2</sub>/EOGF based cell has a characteristic frequency as high as 15 Hz at the phase angle of -45°, or a relaxation time constant of 66.7 ms [53,54]. This relaxation time is much smaller than those of supercapacitors based on carbon nanotube and (Ni, Fe, Co) metal oxide nano-composite [55], graphene and cobalt hydroxide composite [56], manganese oxide and carbon nanotube nano-composite [57], three dimensional graphene coated with manganese oxide [58] and even graphene [54,59]. Synergistic effect of high conductivity of EOGF, tight binding between EOGF and VO<sub>2</sub> particles, large interfacial area between electrolyte and VO<sub>2</sub> particles and small size of VO<sub>2</sub> particles might contribute to their remarkable high frequency response and small relaxation time constant. The result further demonstrates that EOGF is a promising framework to support active materials to build high rate electrochemical energy storage devices.

#### 4. Conclusion

In summary, the VO<sub>2</sub>/EOGF nanostructured electrode based LIBs displays high-rate charge and discharge performancedue to the high electronic and ionic conduction, porous nanostructure and large surface area of this unique nanostructure. Contribution of non-diffusion-limited pseudocapacitance to the capacity is prominent at high rates. Similarly, VO<sub>2</sub>/EOGF electrode based supercapacitors also exhibit rapid response. In particular, the supercapacitor has a characteristic

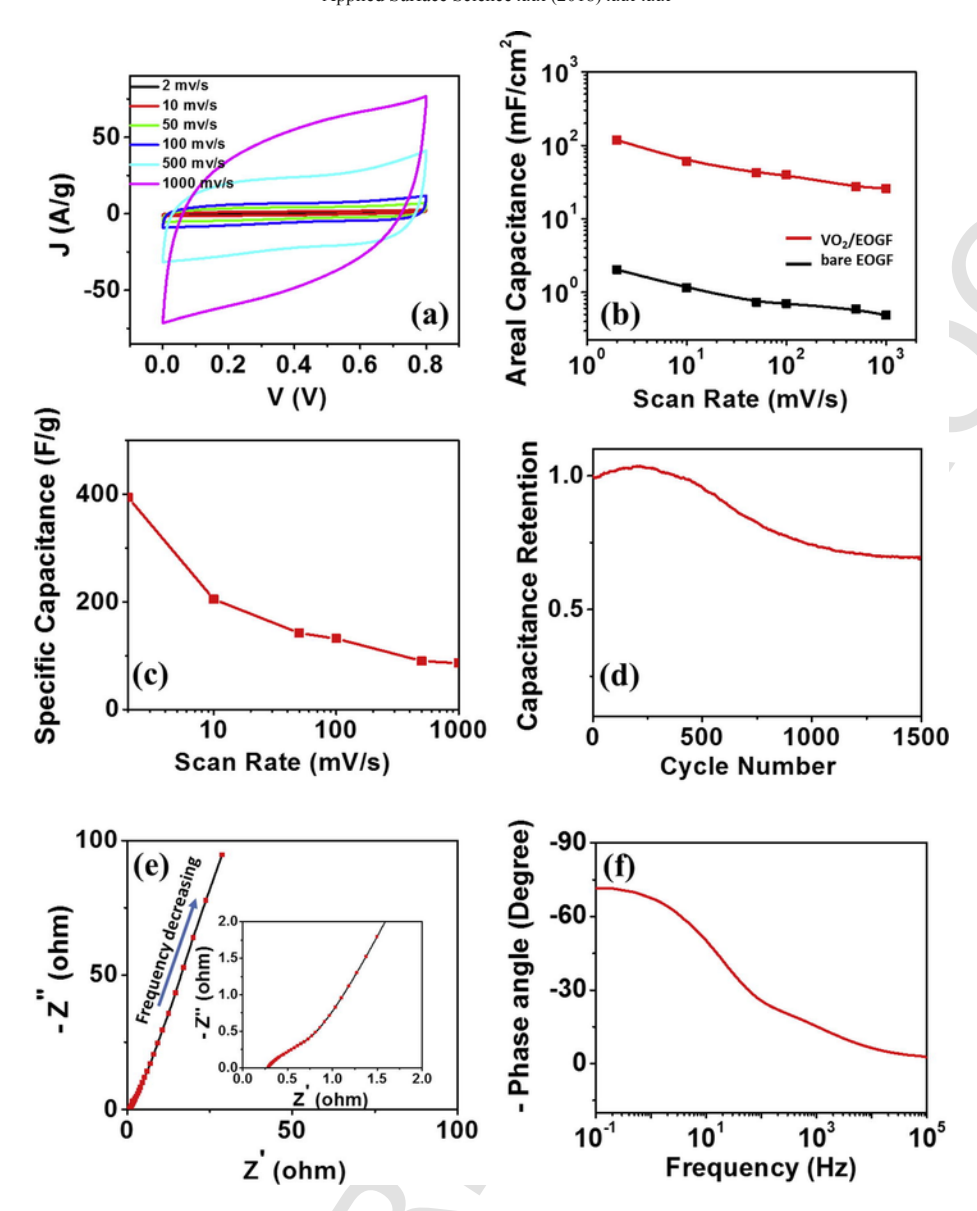


Fig. 4. (a) CV curves of capacitors based on  $VO_2/EOGF$ . (b) Areal capacitance of  $VO_2/EOGF$  and bare EOGF electrodes. (c) Specific capacitance of  $VO_2$ . (d) Capacitance retention of capacitors based on  $VO_2/EOGF$ . (e) Nyquist plot and (f) Bode plot of supercapacitors based on  $VO_2/EOGF$  electrodes.

frequency of 15 Hz when the phase angle reaches -45°, or a relaxation time constant of 66.7 ms. These results suggest that EOGF, produced by depositing EOG on Ni foam, is a superior 3D scaffold in supporting oxide nanomaterials for high-rate electrochemical energy storage and other applications.

#### Acknowledgements

This work was partially supported by National Science Foundation (1611060). Z.F also acknowledges the support from GLEAMM Spark Fund.

#### Appendix A. Supplementary material

Supplementary data associated with this article can be found, in the online version, at https://doi.org/10.1016/j.apsusc.2018.02.059.

#### References

- X. Pan, G. Ren, M.N.F. Hoque, S. Bayne, K. Zhu, Z. Fan, Fast Supercapacitors based on graphene-bridged V<sub>2</sub>O<sub>3</sub>/VOx core-shell nanostructure electrodes with a power density of 1 MW kg<sup>-1</sup>, Adv. Mater. Interfaces 1 (2014) 1400398.
   S.-W. Lee, C.-W. Lee, S.-B. Yoon, M.-S. Kim, J.H. Jeong, K.-W. Nam, K.C.
- [2] S.-W. Lee, C.-W. Lee, S.-B. Yoon, M.-S. Kim, J.H. Jeong, K.-W. Nam, K.C. Roh, K.-B. Kim, Superior electrochemical properties of manganese dioxide/reduced graphene oxide nanocomposites as anode materials for high-performance lithium ion batteries, J. Power Sources 312 (2016) 207–215.
- [3] X. Gu, F. Wu, B. Lei, J. Wang, Z. Chen, K. Xie, Y. Song, D. Sun, L. Sun, H. Zhou, F. Fang, Three-dimensional nitrogen-doped graphene frameworks anchored with bamboo-like tungsten oxide nanorods as high performance anode materials for lithium ion batteries, J. Power Sources 320 (2016) 231–238.
- [4] H.-M. Lee, G.H. Jeong, D.W. Kang, S.-W. Kim, C.-K. Kim, Direct and environmentally benign synthesis of manganese oxide/graphene composites from graphite for electrochemical capacitors, J. Power Sources 281 (2015) 44–48.
- [5] H.-K. Kim, D. Mhamane, M.-S. Kim, H.-K. Roh, V. Aravindan, S. Madhavi, K.C. Roh, K.-B. Kim, TiO<sub>2</sub>-reduced graphene oxide nanocomposites by microwave-assisted forced hydrolysis as excellent insertion anode for Li-ion battery and capacitor, J. Power Sources 327 (2016) 171–177.

- [6] M. Jana, S. Saha, P. Samanta, N.C. Murmu, N.H. Kim, T. Kuila, J.H. Lee, A successive ionic layer adsorption and reaction (SILAR) method to fabricate a layer-by-layer (LbL) MnO<sub>2</sub>-reduced graphene oxide assembly for supercapacitor application, J. Power Sources 340 (2017) 380–392.
- [7] B. Yan, X. Li, Z. Bai, L. Lin, G. Chen, X. Song, D. Xiong, D. Li, X. Sun, Superior sodium storage of novel VO<sub>2</sub> nano-microspheres encapsulated into crumpled reduced graphene oxide, J. Mater. Chem. A 5 (2017) 4850–4860.
- [8] D. Wang, R. Zhang, J. Li, X. Hao, C. Ding, L. Zhao, G. Wen, J. Liu, W. Zhou, General synthesis of graphene-supported bicomponent metal monoxides as alternative high-performance Li-ion anodes to binary spinel oxides, J. Mater. Chem. A 5 (2017) 1687–1697.
- [9] G. Yilmaz, X. Lu, G.W. Ho, Cross-linker mediated formation of sulfur-functionalized V<sub>2</sub>O<sub>5</sub>/graphene aerogels and their enhanced pseudocapacitive performance, Nanoscale 9 (2017) 802–811.
- [10] A. Shoaib, Y. Huang, J. Liu, J. Liu, M. Xu, Z. Wang, R. Chen, J. Zhang, F. Wu, Ultrathin single-crystalline TiO<sub>2</sub> nanosheets anchored on graphene to be hybrid network for high-rate and long cycle-life sodium battery electrode application, J. Power Sources 342 (2017) 405–413.
- [11] Z. Chen, W. Ren, L. Gao, B. Liu, S. Pei, H.-M. Cheng, Three-dimensional flexible and conductive interconnected graphene networks grown by chemical vapour deposition, Nat. Mater. 10 (2011) 424–428.
- [12] Y. He, W. Chen, X. Li, Z. Zhang, J. Fu, C. Zhao, E. Xie, Freestanding three-dimensional graphene/MnO<sub>2</sub> composite networks as ultralight and flexible supercapacitor electrodes, ACS Nano 7 (2012) 174–182.
- [13] K. Xi, P.R. Kidambi, R. Chen, C. Gao, X. Peng, C. Ducati, S. Hofmann, R.V. Kumar, Binder free three-dimensional sulphur/few-layer graphene foam cathode with enhanced high-rate capability for rechargeable lithium sulphur batteries, Nanoscale 6 (2014) 5746–5753.
- [14] M. Yu, Y. Ma, J. Liu, S. Li, Polyaniline nanocone arrays synthesized on three-dimensional graphene network by electrodeposition for supercapacitor electrodes, Carbon 87 (2015) 98–105.
- [15] D. Chao, C. Zhu, X. Xia, J. Liu, X. Zhang, J. Wang, P. Liang, J. Lin, H. Zhang, Z.X. Shen, H.J. Fan, Graphene quantum dots coated VO<sub>2</sub> arrays for highly durable electrodes for Li and Na Ion batteries, Nano Lett. 15 (2015) 565–573.
- [16] K. Yu, Z. Wen, H. Pu, G. Lu, Z. Bo, H. Kim, Y. Qian, E. Andrew, S. Mao, J. Chen, Hierarchical vertically oriented graphene as a catalytic counter electrode in dye-sensitized solar cells, J. Mater. Chem. A 1 (2013) 188–193.
- [17] X. Pan, K. Zhu, G. Ren, N. Islam, J. Warzywoda, Z. Fan, Electrocatalytic properties of a vertically oriented graphene film and its application as a catalytic counter electrode for dye-sensitized solar cells, J. Mater. Chem. A 2 (2014) 12746–12753.
- [18] J.R. Miller, R.A. Outlaw, B.C. Holloway, Graphene double-layer capacitor with ac line-filtering performance, Science 329 (2010) 1637–1639.
- [19] G. Ren, S. Li, Z.-X. Fan, M.N.F. Hoque, Z. Fan, Ultrahigh-rate supercapacitors with large capacitance based on edge oriented graphene coated carbonized cellulous paper as flexible freestanding electrodes, J. Power Sources 325 (2016) 152–160
- [20] M. Cai, R.A. Outlaw, S.M. Butler, J.R. Miller, A high density of vertically-oriented graphenes for use in electric double layer capacitors, Carbon 50 (2012) 5481–5488.
- [21] X. Xiao, P. Liu, J.S. Wang, M. Verbrugge, M.P. Balogh, Vertically aligned graphene electrode for lithium ion battery with high rate capability, Electrochem. Commun. 13 (2011) 209–212.
- [22] G. Ren, M.N.F. Hoque, X. Pan, J. Warzywoda, Z. Fan, Vertically aligned VO<sub>2</sub>(B) nanobelt forest and its three-dimensional structure on oriented graphene for energy storage, J. Mater. Chem. A 3 (2015) 10787–10794.
- [23] G. Ren, S. Li, Z.-X. Fan, J. Warzywoda, Z. Fan, Soybean-derived hierarchical porous carbon with large sulfur loading and sulfur content for high-performance lithium-sulfur batteries, J. Mater. Chem. A 4 (2016) 16507–16515.
- [24] G. Ren, M.N.F. Hoque, J. Liu, J. Warzywoda, Z. Fan, Perpendicular edge oriented graphene foam supporting orthogonal TiO<sub>2</sub>(B) nanosheets as freestanding electrode for lithium ion battery, Nano Energy 21 (2016) 162–171.
- [25] G. Ren, X. Pan, S. Bayne, Z. Fan, Kilohertz ultrafast electrochemical supercapacitors based on perpendicularly-oriented graphene grown inside of nickel foam, Carbon 71 (2014) 94–101.
- [26] S.D. Perera, A.D. Liyanage, N. Nijem, J.P. Ferraris, Y.J. Chabal, K.J. Balkus Jr, Vanadium oxide nanowire—Graphene binder free nanocomposite paper electrodes for supercapacitors: a facile green approach, J. Power Sources 230 (2013) 130–137.
- [27] S. Boukhalfa, K. Evanoff, G. Yushin, Atomic layer deposition of vanadium oxide on carbon nanotubes for high-power supercapacitor electrodes, Energy Environ. Sci. 5 (2012) 6872–6879.
- [28] M. Sathiya, A. Prakash, K. Ramesha, J.M. Tarascon, A. Shukla, V<sub>2</sub>O<sub>5</sub>-anchored carbon nanotubes for enhanced electrochemical energy storage, J. Am. Chem. Soc. 133 (2011) 16291–16299.
- [29] A. Pan, H.B. Wu, L. Yu, X.W.D. Lou, Template-free synthesis of VO<sub>2</sub> hollow microspheres with various interiors and their conversion into V2O5 for lithium-ion batteries, Angewandte Chemie 125 (2013) 2282–2286.

- [30] J. Xie, C. Wu, S. Hu, J. Dai, N. Zhang, J. Feng, J. Yang, Y. Xie, Ambient rutile VO<sub>2</sub>(R) hollow hierarchitectures with rich grain boundaries from new-state nsutite-type VO<sub>2</sub>, displaying enhanced hydrogen adsorption behavior, PCCP 14 (2012) 4810–4816.
- [31] G. Li, K. Chao, C. Zhang, Q. Zhang, H. Peng, K. Chen, Synthesis of urchin-like VO<sub>2</sub> nanostructures composed of radially aligned nanobelts and their disassembly, Inorg. Chem. 48 (2009) 1168–1172.
- [32] X.C. Dong, Y.M. Shi, Y. Zhao, D.M. Chen, J. Ye, Y.G. Yao, F. Gao, Z.H. Ni, T. Yu, Z.X. Shen, Y.X. Huang, P. Chen, L.J. Li, Symmetry Breaking of Graphene monolayers by molecular decoration, Phys. Rev. Lett. 102 (2009) 135501.
- [33] A.C. Ferrari, J.C. Meyer, V. Scardaci, C. Casiraghi, M. Lazzeri, F. Mauri, S. Piscanec, D. Jiang, K.S. Novoselov, S. Roth, A.K. Geim, Raman spectrum of graphene and graphene layers, Phys. Rev. Lett. 97 (2006) 187401.
- [34] A.C. Ferrari, Raman spectroscopy of graphene and graphite: disorder, electron-phonon coupling, doping and nonadiabatic effects, Solid State Commun. 143 (2007) 47–57.
- [35] J. Wei, H. Ji, W. Guo, A.H. Nevidomskyy, D. Natelson, Hydrogen stabilization of metallic vanadium dioxide in single-crystal nanobeams, Nat. Nanotechnol. 7 (2012) 357–362.
- [36] S. Zhang, J.Y. Chou, L.J. Lauhon, Direct correlation of structural domain formation with the metal insulator transition in a VO<sub>2</sub> nanobeam, Nano Lett. 9 (2009) 4527–4532.
- [37] G. Petrov, V. Yakovlev, J. Squier, Raman microscopy analysis of phase transformation mechanisms in vanadium dioxide, Appl. Phys. Lett. 81 (2002) 1023–1025.
- [38] C. Niu, J. Meng, C. Han, K. Zhao, M. Yan, L. Mai, VO<sub>2</sub> Nanowires assembled into hollow microspheres for high-rate and long-life lithium batteries, Nano Lett. 14 (2014) 2873–2878.
- [39] L. Mai, Q. Wei, Q. An, X. Tian, Y. Zhao, X. Xu, L. Xu, L. Chang, Q. Zhang, Nanoscroll buffered hybrid nanostructural VO<sub>2</sub>(B) cathodes for high-rate and long-life lithium storage, Adv. Mater. 25 (2013) 2969–2973.
- [40] Y.W. Zhu, S. Murali, M.D. Stoller, K.J. Ganesh, W.W. Cai, P.J. Ferreira, A. Pirkle, R.M. Wallace, K.A. Cychosz, M. Thommes, D. Su, E.A. Stach, R.S. Ruoff, Carbon-based supercapacitors produced by activation of graphene, Science 332 (2011) 1537–1541.
- [41] H. Liu, Y. Wang, K. Wang, E. Hosono, H. Zhou, Design and synthesis of a novel nanothorn VO<sub>2</sub>(B) hollow microsphere and their application in lithium-ion batteries, J. Mater. Chem. 19 (2009) 2835–2840.
- [42] D. Wang, D. Choi, J. Li, Z. Yang, Z. Nie, R. Kou, D. Hu, C. Wang, L.V. Saraf, J. Zhang, Self-assembled TiO<sub>2</sub>-graphene hybrid nanostructures for enhanced Li-ion insertion, ACS Nano 3 (2009) 907–914.
- [43] C. Nethravathi, C.R. Rajamathi, M. Rajamathi, U.K. Gautam, X. Wang, D. Golberg, Y. Bando, N-doped graphene–VO<sub>2</sub>(B) nanosheet-built 3D flower hybrid for lithium ion battery, ACS Appl. Mater. Interfaces 5 (2013) 2708–2714.
- [44] X. Zhu, Y. Zhu, S. Murali, M.D. Stoller, R.S. Ruoff, Nanostructured reduced graphene oxide/Fe<sub>2</sub>O<sub>3</sub> composite as a high-performance anode material for lithium ion batteries, Acs Nano 5 (2011) 3333–3338.
- [45] Z.-S. Wu, W. Ren, L. Wen, L. Gao, J. Zhao, Z. Chen, G. Zhou, F. Li, H.-M. Cheng, Graphene anchored with Co<sub>3</sub>O<sub>4</sub> nanoparticles as anode of lithium ion batteries with enhanced reversible capacity and cyclic performance, ACS Nano 4 (2010) 3187–3194.
- [46] C. Lin, B. Ding, Y. Xin, F. Cheng, M.O. Lai, L. Lu, H. Zhou, Advanced electrochemical performance of Li<sub>4</sub>Ti<sub>5</sub>O<sub>12</sub>-based materials for lithium-ion battery: Synergistic effect of doping and compositing, J. Power Sources 248 (2014) 1034–1041.
- [47] X. Huang, H. Yu, J. Chen, Z. Lu, R. Yazami, H.H. Hng, Ultrahigh rate capabilities of lithium-ion batteries from 3D ordered hierarchically porous electrodes with entrapped active nanoparticles configuration, Adv. Mater. 26 (2014) 1296–1303
- [48] X. Pan, Y. Zhao, G. Ren, Z. Fan, Highly conductive VO<sub>2</sub> treated with hydrogen for supercapacitors, Chem. Commun. 49 (2013) 3943–3945.
- [49] Q. Chen, X. Li, X. Zang, Y. Cao, Y. He, P. Li, K. Wang, J. Wei, D. Wu, H. Zhu, Effect of different gel electrolytes on graphene-based solid-state supercapacitors, RSC Adv. 4 (2014) 36253–36256.
- [50] X. Li, T. Zhao, Q. Chen, P. Li, K. Wang, M. Zhong, J. Wei, D. Wu, B. Wei, H. Zhu, Flexible all solid-state supercapacitors based on chemical vapor deposition derived graphene fibers, PCCP 15 (2013) 17752–17757.
- [51] Y. Fu, X. Cai, H. Wu, Z. Lv, S. Hou, M. Peng, X. Yu, D. Zou, Fiber supercapacitors utilizing pen ink for flexible/wearable energy storage, Adv. Mater. 24 (2012) 5713–5718
- [52] Y. Fu, H. Wu, S. Ye, X. Cai, X. Yu, S. Hou, H. Kafafy, D. Zou, Integrated power fiber for energy conversion and storage, Energy Environ. Sci. 6 (2013) 805–812
- [53] P.L. Taberna, P. Simon, J.-F.O. Fauvarque, Electrochemical characteristics and impedance spectroscopy studies of carbon-carbon supercapacitors, J. Electrochem. Soc. 150 (2003) A292–A300.

- [54] M.F. El-Kady, V. Strong, S. Dubin, R.B. Kaner, Laser scribing of high-performance and flexible graphene-based electrochemical capacitors, Science 335 (2012) 1326–1330.
- [55] A.S. Adekunle, K.I. Ozoemena, B.O. Agboola, MWCNTs/metal (Ni Co, Fe) oxide nanocomposite as potential material for supercapacitors application in acidic and neutral media, J. Solid State Electrochem. (2013) 1–10.
- [56] Z. Li, J. Wang, L. Niu, J. Sun, P. Gong, W. Hong, L. Ma, S. Yang, Rapid synthesis of graphene/cobalt hydroxide composite with enhanced electrochemical performance for supercapacitors, J. Power Sources 245 (2014) 224–231.
- [57] S. Zhang, C. Peng, K.C. Ng, G.Z. Chen, Nanocomposites of manganese oxides and carbon nanotubes for aqueous supercapacitor stacks, Electrochimica Acta 55 (2010) 7447–7453.
- [58] B.G. Choi, M. Yang, W.H. Hong, J.W. Choi, Y.S. Huh, 3D macroporous graphene frameworks for supercapacitors with high energy and power densities, ACS Nano 6 (2012) 4020–4028.
- [59] T. Kim, G. Jung, S. Yoo, K.S. Suh, R.S. Ruoff, Activated graphene-based carbons as supercapacitor electrodes with macro-and mesopores, Acs Nano 7 (2013) 6899–6905.